Extreme Mechanics Letters 17 (2017) 7–15

Contents lists available at ScienceDirect

Extreme Mechanics Letters

journal homepage: www.elsevier.com/locate/eml

Asymmetric energy barrier and mechanical diode effect from folding multi-stable stacked-origami

Hongbin Fang [a], K.W. Wang [a], Suyi Li [b,*]

[a] Department of Mechanical Engineering, University of Michigan, Ann Arbor, MI, 48109, United States
[b] Department of Mechanical Engineering, Clemson University, Clemson, SC, 29634, United States

ARTICLE INFO

Article history:
Received 29 August 2017
Received in revised form 25 September 2017
Accepted 26 September 2017
Available online 3 October 2017

Keywords:
Multi-stability
Origami
Mechanical diode

ABSTRACT

Origami, the ancient art of paper folding, has evolved into a design framework of a wide variety of engineering systems such as deployable structures and architected cellular materials. The fundamentally three-dimensional folding is not only a capable tool to generate shape transformation, but also a powerful platform to program sophisticated elastic properties. This study investigates the multi-stability characteristics of a stacked origami cellular solid consisting of multiple Miura-ori sheets, specifically focusing on a dual-cell chain structure. Experiment results indicate that folding imposes a unique kinematic constraint between the two adjacent bistable origami cells, which can significantly increase the energy barrier of the extensional switch from one stable state to another without notably increasing the barrier of the opposite switch, creating an asymmetric barrier. We formulate a geometric mechanics model to examine the underlying physical principles of the observed asymmetric behaviors, and demonstrate the potentials to strengthen this asymmetric energy barrier and to achieve a static mechanical diode effect. That is, the multi-stable origami could be easily compressed via switching between different stable states, but demand a large external force to be extended. Since such diode effect has the potential to rectify reciprocal loads into unidirectional deformation, the results of this study can become the building blocks for origami solids with novel functionalities.

1. Introduction

Multi-stable materials and structures – characterized by the coexisting elastic energy minima within their deformation range – have garnered extensive interests recently because they can provide a wide spectrum of adaptive functions. To begin, their capability of remaining at different configurations without external aids makes them immediately appealing for the use in shape morphing and actuation [1–4]. Secondly, multi-stable materials and structures can exhibit different mechanical properties at different stable equilibria (or states), thus one can strategically switch them among their stable states for performance tuning. Stiffness [5–8] and auxetic property [9] adaptation have been demonstrated by this strategy. Furthermore, multi-stability can also lead to high performance dynamic functions [10], including vibration control [11–14], energy harvesting [15–17], and robust sensing [18,19]. Especially, a chain-like structure consisting of many bistable elements connected in series can achieve strain-rate-independent and recoverable impact energy absorption [20–25], deterministic deformation sequence [26], and even non-reciprocal wave propagation [27,28]. Therefore, incorporating multi-stability is one of the most promising and powerful strategies for creating adaptive structures and functional materials.

Despite the vast variety in these multi-functional structures and materials, the underlying mechanisms of multi-stability are similar. Most of the current systems are built upon either curved bistable beams or their close relatives such as pre-stressed bilayer shells and axially constrained springs. The deformation mechanism of the curved beams is planar, and the corresponding bistability is evident only in one direction (aka. one-dimensional). Such simplicity permits the rapid application of established tools for mechanics analysis, performance evaluation, and reliable fabrication. However, it is also a significant limiting factor in terms of the overall potentials. Although space-filling lattices were assembled based on the curved beams [23,29], their overall stability characteristics remain essentially the same. Evolution to a truly three-dimensional system may serve as a platform through which we would discover new multi-stability characteristics and functionalities that are not available in the lower-dimensional systems.

To address this gap, we explore the utilization of origami, a fundamentally three-dimensional shape transformation mechanism, as the underlying architecture of multi-stable materials and structures. Developed in Asia approximately four centuries ago, origami

* Corresponding author.
E-mail address: suyil@clemson.edu (S. Li).

https://doi.org/10.1016/j.eml.2017.09.008
2352-4316/

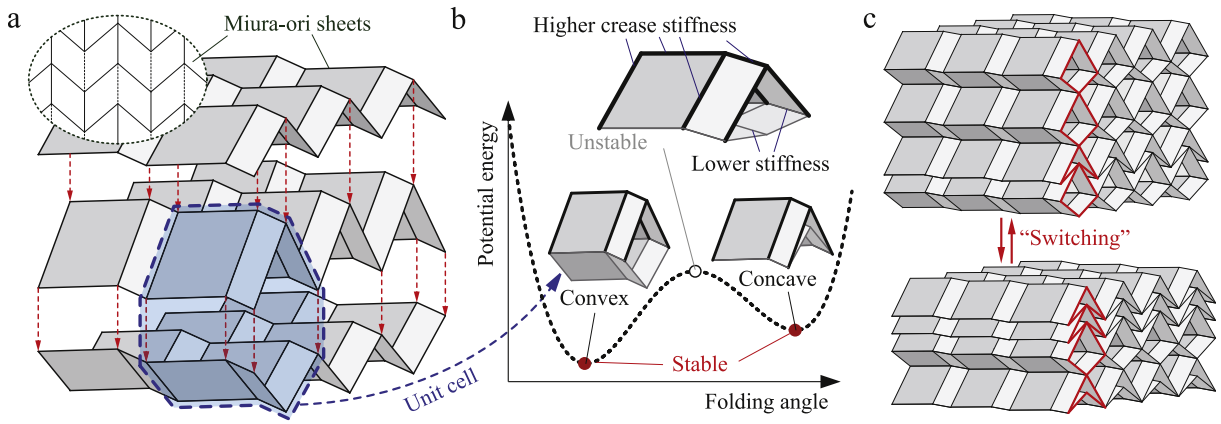

Fig. 1. The concept of multi-stable cellular solid based on stacked origami. (a) Stacking and connecting translational periodic origami sheets, such as the classic Miura-ori, can form a space filling architecture; (b) prescribed differences in the crease torsional stiffness can generate bistability in each unit cell; and (c) stacked origami consisting of many unit cells can possess multiple stable states with different internal configurations, which can be switched via different actuation mechanisms.

is the art of folding paper into decorative shapes and geometries [30]. Over the last several decades, this craftsman art quickly evolved into a sophisticated framework for designing and fabricating engineered systems such as deployable aerospace structures [31], kinetic architectures [32–34], self-folding robots [35–37], and biomedical devices [38,39]. Especially, origami sheets with a translational periodic morphology can be stacked and connected to form an architected cellular solid with mechanical properties dominated by the kinematics of folding [40–48]. Such a stacked origami cellular solid (referred as *stacked origami* in what follows) is essentially a three-dimensional assembly of the "unit cells", which consist of two different origami sheets (Fig. 1(a)). With compatible crease designs, the unit cells and the overall stacked origami can be rigid-foldable [42,47], meaning that their folding can be simplified into rigid panels rotating around the crease lines. Therefore, the overall elastic properties of the stacked-origami can be characterized based on the torsional stiffness of the crease lines. In particular, if the crease torsional stiffness of the two constituent origami sheets differ notably, bistability will occur (Fig. 1(b)) [49]. As a result, the stacked origami can exhibit many stable states with different internal folding configurations (Fig. 1(c)).

Multi-stability has been investigated in single Origami sheets [50–53], but the stacked origami in this study is unique in that it exhibits unique stability properties that are not observed in lower-dimensional systems [54]. In this letter, we report an experimental examination and in-depth investigation of the unorthodox asymmetric energy barrier: the folding-induced kinematic constraint between adjacent unit cells can significantly increase the energy barrier of switching from one stable state to another, without imposing notable changes to energy barrier of the opposite switch. As a result, the stacked origami is relatively easy to be compressed via switching but requires a much larger force to be extended. Furthermore, we show that such asymmetric behavior can be strengthened to a static mechanical diode effect. Results of this study can potentially open up new avenues toward multifunctional materials and structures that are capable of motion rectifying and wave propagation control.

The following sections of this Letter will (1) briefly review the origin of bistability in a single origami unit cell; (2) present experimental observations on the asymmetric behavior when switching between two stable states; (3) examine the underlying physical principles of the asymmetric energy barrier and the potential to achieve static diode effect; (4) discuss the correlations between the asymmetric energy barrier and origami design.

2. Bistability of the unit cell

The unit cell shown in Fig. 2(a) is the fundamental element to achieve multi-stability. Its external geometries can be fully defined by two types of parameters [42]. One is the geometric designs parameters of the constituent Miura-ori sheets including the crease lengths (a_k and b_k) and sector angle (γ_k), where the subscript k (='I' or 'II') denotes the sheets I and sheet II, respectively. The other type of parameters is the folding angle θ_k, defined as the dihedral angles between the facets and the x-y reference plane. The rigid-folding condition is satisfied when $b_{\mathrm{I}} = b_{\mathrm{II}}$, $a_{\mathrm{I}} \cos\gamma_{\mathrm{I}} = a_{\mathrm{II}} \cos\gamma_{\mathrm{II}}$, and $\cos\theta_{\mathrm{I}} \tan\gamma_{\mathrm{I}} = \cos\theta_{\mathrm{II}} \tan\gamma_{\mathrm{II}}$ [42,49]. In this way, we can assume that the origami facets are rigid and the creases act like hinges with prescribed torsional stiffness. Moreover, folding of the unit cell is a one-degree-of-freedom mechanism so that we can use the sheet I folding angle θ_{I} (denoted simply as θ in what follows) as the independent variable to describe the overall folding process. Such seemingly simple assumption is indeed capable of revealing the underlying physical principles behind many folding-induced, nonlinear elastic properties without unnecessary complexities [41,55–57]. Denoting φ_i as the dihedral opening angles of the creases shown in Fig. 2(a), and K_i as the corresponding crease torsional stiffness, the total elastic potential energy of the unit cell is a summation of the individual crease energy so that

$$\Pi = \frac{1}{2}\sum_{i=1}^{5} K_i\left(\varphi_i - \varphi_i^{\mathrm{o}}\right)^2, \tag{1}$$

where φ_i are functions of folding angle θ :

$$\sin\frac{\varphi_2}{2} = \frac{\cos\theta}{\sqrt{1-\sin^2\theta\sin^2\gamma_{\mathrm{I}}}}, \tag{2}$$

$$\sin\frac{\varphi_4}{2} = \frac{\sin\gamma_{\mathrm{I}}}{\sin\gamma_{\mathrm{II}}}\sin\frac{\varphi_2}{2}, \tag{3}$$

and $\varphi_1 = \pi - 2\theta$, $\varphi_3 = \pi - 2\cos^{-1}\left(\tan\gamma_{\mathrm{II}}\tan^{-1}\gamma_{\mathrm{I}}\cos\theta\right)$, $\varphi_5 = \cos^{-1}\left(\tan\gamma_{\mathrm{II}}\tan^{-1}\gamma_{\mathrm{I}}\cos\theta\right) - \theta$. φ_i^{o} in Eq. (1) are the crease opening angles corresponding to the stress-free stable state ($\theta = \theta_{\mathrm{o}}$) at which no creases are subject to deformation. K_i in Eq. (1) can be calculated as $K_1 = 2k_{\mathrm{I}}b_{\mathrm{I}}$, $K_2 = 2k_{\mathrm{I}}a_{\mathrm{I}}$, $K_3 = 2k_{\mathrm{II}}b_{\mathrm{I}}$, $K_4 = 2k_{\mathrm{II}}a_{\mathrm{II}}$, and $K_5 = 4k_c b_{\mathrm{I}}$, where k_{I}, k_{II}, and k_c are the torsional stiffness *per unit length* of the sheet I crease, sheet II crease, and the connecting crease, respectively. The numerical constants in these stiffness expressions denote the number of creases that have the same opening angle in a unit cell.

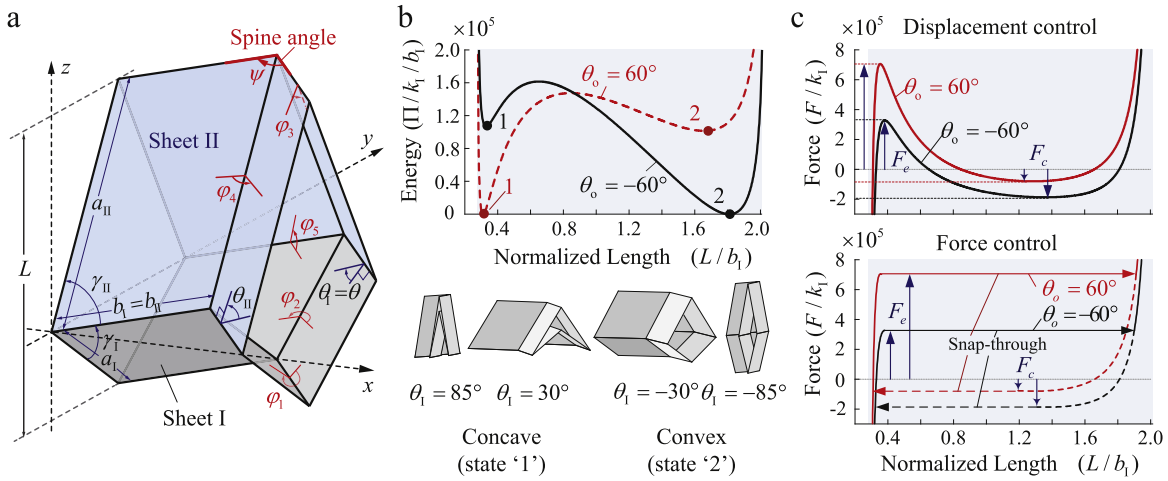

Fig. 2. Bistability of the unit cell in the stacked origami architecture. (a) The external geometry of a unit cell, where the dihedral opening angle φ_i plays an important role in achieving elastic bistability; and the spine angle ψ is related to the kinematic constraints between two adjacent unit cells (introduced in Section 4). (b) Elastic potential energy landscapes of two different unit cells based on two different stress-free folding angles θ_0. The two stable states, denoted by solid circles, will be denoted as state '1' if it has a concave shape, and state '2' otherwise. (c) The force–displacement curves of the two unit cell under displacement control (top) and force control (bottom), the two critical forces (F_e and F_c) of the two cells are highlighted. The shaded region in (b) and (c) represents the admissible deformation range based on rigid folding assumptions.

The external length of the unit cell is also a functions of θ :

$$L = a_1 \sin\gamma_1 \left(\sqrt{\frac{\tan^2\gamma_{II}}{\tan^2\gamma_1} - \cos^2\theta} - \sin\theta \right). \tag{4}$$

The change in potential energy Π with respect to the unit cell length (L) is illustrated in Fig. 2(b). Because of the nonlinear geometric correlations among the folding angle (θ), crease opening angles (φ_i), and the external dimension (L), the effective stiffness of the unit cell is highly nonlinear even though its constituent creases is assumed to be linearly elastic in torsion. The double potential energy wells, which are the defining characteristics of a bistable system, start to show up as the crease torsional stiffness of the sheet II (k_{II}) becomes sufficiently larger than k_1 and k_c, or the stress-free folding angle (θ_o) deviates away from 0° [49]. Fig. 2(b) illustrates the elastic energy landscapes of two different origami unit cell designs that differ in their stress-free folding angles ($\theta_0 = -60°, 60°$) but share the same geometric and crease stiffness designs: $a_1 = b_1$, $a_{II} = 1.25a_1$, $\gamma_1 = 60°$, $k_1 = k_c$, and $k_{II} = 20k_1$. Unless otherwise noted, all of the following case studies in this Letter are based on these design parameters, and interested readers can refer to our previous publication for an in-depth study on the design criteria of obtaining bi-stability [49]. If the stress-free stable state is designed to have a concave shape ($\theta_o > 0$), the other stable one will be convex, and vice versa. For clarity we denote the concave stable equilibrium as state '1' and the convex equilibrium as state '2' (Fig. 2(b)). The corresponding reaction force–displacement curves of the unit cells can be calculated as the variation of energy Π with respect to the changes in cell length (*displacement control*), i.e., $F = d\Pi/dL = (d\Pi/d\theta)\,(dL/d\theta)^{-1}$ (Fig. 2(c)). In these force–displacement curves, two values are important for this study: they are the magnitudes of extension force F_e and the compression force F_c at the critical configurations where negative stiffness occurs. They are the critical forces required to trigger the snap-through switches of the unit cell if a *force control* is applied (Fig. 2(c)). Here the subscript "e" and "c" denote the extension and compression, respectively. Note that the individual unit cell already show asymmetric bistability in terms of their potential energy well depths and widths, as well as the magnitudes of critical forces F_e and F_c. However, we will show that the asymmetry reported in this Letter possesses fundamentally different origin and properties.

Two origami unit cells prototypes are fabricated to experimentally verify the bistability. The origami facets are water jet cut individually, according to the geometric designs in the case studies in Fig. 2, from 0.25 mm thin stainless-steel sheets. They are pasted to a 0.13 mm thick adhesive-back ultra-high molecular weight (UHMW) polyethylene film to form individual Miura-ori sheets. Then two Miura-ori sheets are connected by adhesive films to form a complete origami unit cell. By this construction, the facet material is significantly stiffer than crease material to ensure rigid-foldability. 0.01 mm thick, pre-bent spring-steel stripes are pasted to the creases corresponding to dihedral angles φ_4 to provide high torsional stiffness K_4, thus imparting bistability to each unit cell (Fig. 3). The two unit cell prototypes are fabricated with different amount of spring-steel stripes, and the measured force–displacement relationships are shown in Fig. 3. Although quantitative discrepancies exist between the experiment results and the analytical predictions shown in Fig. 2(c), the qualitative relationship between the critical forces at snap-through configurations are consistent. That is, $F_e^{PA} < F_e^{PB}$ and $F_c^{PA} > F_c^{PB}$, where the superscripts "PA" and "PB" denote the two prototypes of unit cell. Such relationships between critical forces dictate the switching behaviors and mechanical diode effects discussed in the following.

3. Experimental observation of the asymmetric energy barriers in dual-cell chains

We then conducted two different sets of tests to investigate the force–displacement relationships of chain-like structures consisting of the two unit cell prototypes. In the first set, the two cells are connected by a rigid rod so they behave like two bistable elements simply connected in series with a balanced internal force, this setup is essentially the same as in the previous studies of bistable chain structures [20–25]. In the second set of tests, however, the two cells are connected directly along their zig-zag crease lines by adhesive films, this setup is consistent with the staked origami construction shown in Fig. 1. Here we arrange cell A to be always on the top. In both sets, five tension and compression load cycles are conducted, in which the dual-cell chain is first extended from the "concave-concave" (i.e. '1-1') stable state to the "convex-convex" (i.e., '2-2') state, and then compressed back to the '1-1' state (the two numbers in the '*i-j*' notations represent the stable states of cell

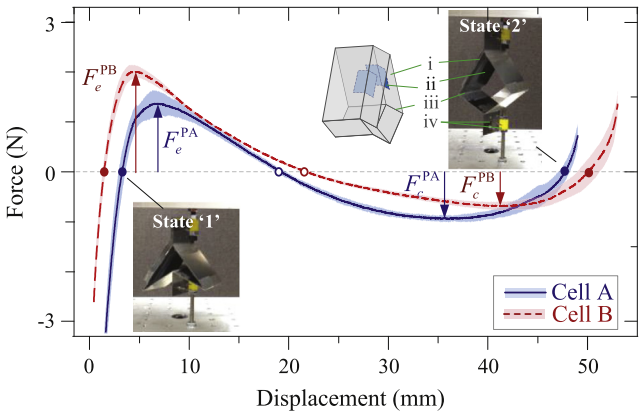

Fig. 3. Measured force–displacement curves of the two unit cell prototypes. Five displacement-controlled tests are repeated for each cell, the solid curves are the averaged results, and the shaded bands represent the standard deviations. Insets show the photos of a cell at states '1' and '2', and illustrate the construction of the unit cell, where (i) is the steel facets, (ii) is the pre-bent spring-steel stripes, (iii) is the creases made of plastic film, and (iv) is the additional rectangular steel plates and 3D-printed connectors for connecting with the universal testing machine.

A and cell B, respectively). Displacement control with a constant crosshead speed (10 mm/min) is used in these tests.

Fig. 4(a) shows the averaged extension and compression test data. The dual-cell chain, regardless of the inter-cellular connection, possesses four stable states: '1-1', '2-1', '2-2' and '1-2'. However, test results show that only the first three of them can be reached via displacement control at the two ends of the chain (Fig. 4(b, c)). The differences in the critical forces of a single cell (i.e. F_e^{PA}, F_c^{PA}, F_e^{PB}, and F_c^{PB}) can explain the absence of the '1-2' stable state in the tests. During extension, the top cell A always "bulges out" first because its corresponding critical force for snap-out deformation (F_e^{PA}) is lower than that of bottom cell B (F_e^{PB}) (Fig. 3), incurring a switch sequence of '1-1'→'2-1'→'2-2'. During compression, the bottom cell B always "nests in" first because its critical force for snap-in deformation (F_c^{PB}) is lower than that of top cell A (F_c^{PA}), incurring a switch sequence of '2-2'→'2-1'→'1-1'. The above switches are evidenced by the negative slopes in the force–displacement curves (i.e., negative stiffness).

Despite exhibiting the same switching sequence between stable states, the two sets of tests show a significant difference in terms of the magnitudes of critical force for switching, especially between the '2-1' and '2-2' stable states. The critical force corresponding to the extensional '2-1'→'2-2' switch is considerably higher in the film connected tests (i.e. $F_e^{\mathrm{F}} > F_e^{R}$ in Fig. 4); however, the critical forces corresponding to the opposite '2-2'→'2-1' switch are similar between the two types of inter-cellular connections. Here the superscript "R" and "F" represent the rod-connected and film-connected tests, respectively. More specifically, in the film-connected dual cell chain, the ratio of the critical forces $F_e^{\mathrm{F}}/F_c^{\mathrm{F}} = 7.21$, while in the rod-connected chain $F_e^{\mathrm{R}}/F_c^{\mathrm{R}} = 3.42$.

Since the only difference between the two sets of tests is the connection between the two bistable cells, the observed differences in critical forces imply that the film connection can significantly increase the potential energy barrier for the extension switch from "2-1" to "2-2", however, it does not impose any notable changes to the energy barrier of the opposite compression switch. This surprising asymmetric behavior necessitates an in-depth examination on the underlying physical principles, which is discussed in the following sections.

4. Origin of the asymmetric energy barriers and the potential of achieving static diode effect

The two different types of inter-cellular connection generate fundamentally different deformation mechanisms. With the rod connection, the deformations of constituent bistable cells are independent with respect to each other, as long as the internal forces between them are balanced. However, with the film connection, deformations of the unit cells are instead directly coupled due to a kinematic constraint from the zig-zag connecting creases. Define a "spine" angle $\psi = 2\tan^{-1}(\cos\theta\tan\gamma_1)$ corresponding to the connecting creases (Fig. 5(a)). If the rigid-folding assumptions are strictly followed (i.e. rigid origami facets and hinge-like creases), the spine angle associated to the zig-zag crease should be identical between the two cells during the entire folding process so that

$$\psi^{\mathrm{A}} = \psi^{\mathrm{B}}. \tag{5}$$

As a result, the folding angles of the two unit cells are not independent but rather follow the relationship:

$$\theta^{\mathrm{A}} = \pm\theta^{\mathrm{B}}. \tag{6}$$

This relationship implies that folding of the ideally rigid dual-cell chain possesses only one degree-of-freedom for folding, and the corresponding *admissible* deformations are restricted to the two paths shown in Fig. 5(b), where the total length of the dual-cell chain $L^{\mathrm{t}} = L^{\mathrm{A}} + L^{\mathrm{B}}$. The two unit cells have the same folding angle on one path ("a-b"), or the opposite folding angles on the other path ("c-d"). These two paths meet at the point of $\theta^{\mathrm{A}} = \theta^{\mathrm{B}} = 0$, where the bottom sheets (i.e., Miura-ori sheets I) in both cells are flat (position "o" in Fig. 5(b, c)).

However, close observations on the dual-cell prototypes suggests that such ideal rigid-folding constraint cannot be fully achieved due to fabrication errors and crease compliance. For a more in-depth examination on the experiment observations, we relax the constraint condition in Eq. (5) by allowing the spine angles of the two cells to mismatch. In this way, the admissible deformation of the dual cell chain would be able to cover the entire parallelogram in Fig. 5(b). However, such mismatch will induce extra constraint energy

$$\Pi^* = \frac{1}{2}k^* b_1\left(\psi^{\mathrm{A}} - \psi^{\mathrm{B}}\right)^2, \tag{7}$$

where k^* is an equivalent stiffness per unit length associated to the strength of the deformation coupling from the zig-zag connecting creases. The total energy Π^{t} of the dual cell chain is therefore the combination of the elastic crease folding energy Π (defined in Eq. (1)) and Π^* so that

$$\Pi^{\mathrm{t}} = \Pi_k^{\mathrm{A}} + \Pi_k^{\mathrm{B}} + \Pi^*. \tag{8}$$

The effective magnitude of k^* is related to many factors such as the stacked origami construction method and the material used. It is worth emphasizing that, the interest of this study is not on the accurate calculation of k^*, but rather on how the *changes in the magnitude of* k^* can influence the overall elastic behaviors of the dual-cell chain. In this way, we can obtain the physical insights on how this kinematic constraint originated from folding induces the asymmetric behaviors observed in the experiment.

We first study a special case that the effective stiffness k^* is zero, i.e., there is no constraint between the spine angles ψ^{A} and ψ^{B} so that the two unit cells are simply connected in series. Such case is consistent with the rod-connected tests. Fig. 6 plots the energy landscape and the force–displacement curves based on (Eq. (8)), where the designs of the two unit cells are the same as in the case studies shown in Fig. 2. The energy contour map in Fig.

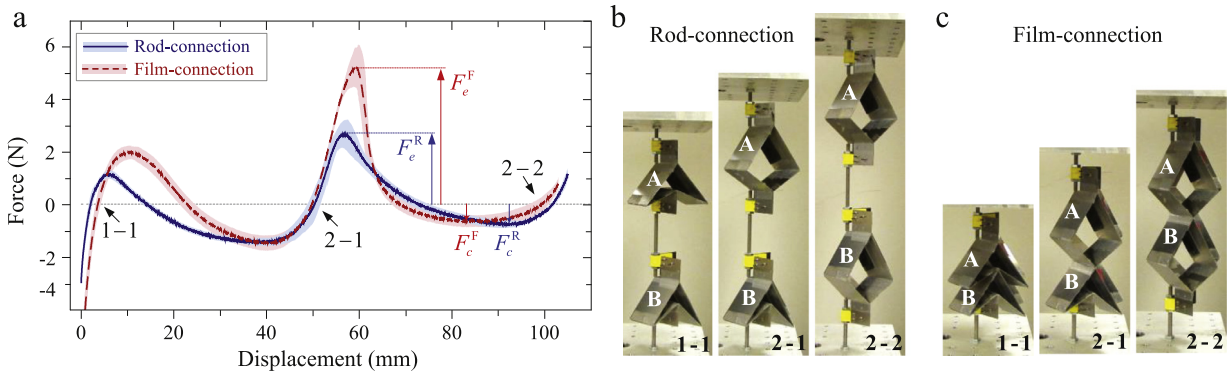

Fig. 4. Tension and compression tests on dual-cell chain prototypes with different types of connection between the two bistable cells. (a) Force–displacement curves of the two sets of tests based on displacement-controlled method. The solid and dashed curves are the averaged test results, and the shaded bands are the standard deviations. Photos of the rod-connected test (b) and the film-connected test (c) shows three stable states ('1-1', '2-1', and '2-2').

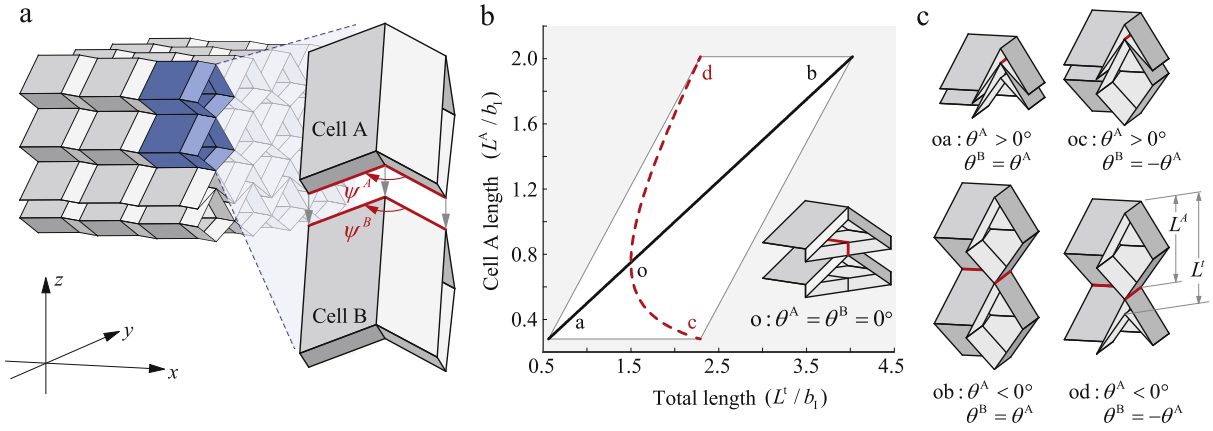

Fig. 5. Kinematics of a dual-cell chain. (a) Assembling two unit cells together requires equal spine angles between these two: $\psi^A = \psi^B$. (b) Due to this kinematic constraint, folding configurations of the two cells are not independent, and they must lie on the two paths of admissible deformations in terms of their lengths. The parallelogram is the range of admissible deformations without the kinematic constraints from the connecting creases; and the shaded regions are physically unachievable. (c) Illustrations of different folding configurations along the two kinematic paths.

6(a) shows two "potential energy paths" found by identifying the energy minima corresponding to a given total chain length L^t. Among the two paths, one connects three stable states '1-1', '2-1', and '2-2'. Therefore, if the dual-cell chain is initially settled at any one of these three stable states, extending or compressing the dual-cell chain can switch it to any other two states. The reaction forces associated to such switches, calculated as the derivative of the total energy Π^t with respect to the change in overall chain length L^t, is shown in Fig. 6(c). This subplot represents the quasi-static response of this dual-cell chain based on displacement control. Fig. 6(d) represents the responses based on force control, showing the chain deformation corresponding to prescribed external forces as well as the multiple "snap-through" behaviors occurring at the onset of elastic instability. Here, similar to the notation in experiments, we denote F_e as the required extension force to achieve snap-through from the '2-1' state toward the '2-2' state, and F_c as the required compression force to achieve the opposite snap-through. In this particular case, the energy path that includes the '1-2' stable state is disconnected from others. Therefore, the dual-cell chain cannot be extended or compressed to the '1-2' state by displacement control at the both ends, which is consistent with our experimental observation. To avoid unnecessary complexities, this path will be omitted in the following study.

As the equivalent constraint stiffness k^* increases, the energy landscape of the dual cell chain changes accordingly (Fig. 7, first two rows). If the constraint stiffness is large enough (e.g. $k^*/k_l = 320$ in Fig. 7(c), k_l is the crease torsional stiffness per unit length of the Miura-ori sheet I), the multi-stability characteristics of the overall dual-cell chain become fundamentally different: the originally continuous energy path that connects the three stable states splits into two separate ones. Such a split occurs between the '2-1' and '2-2' states, and the two separated paths can overlap within the same range of total chain length, thus creating the asymmetric energy barrier. Starting from the stable '2-1' state, when the dual-cell chain is monotonically extended by displacement control, it will deform by following the energy path until the position 'p' shown in Fig. 7(d), then it will jump to the other energy path at position 'q'. During this jump, the internal folding configuration of the dual cell chain and the reaction force will change significantly even though the total chain length changes little. On the other hand, if the dual-cell chain is compressed monotonically from the '2-2' stable state, it will deform to a different position 'r' before jumping to 's'. Note that such jumps are achieved with displacement control rather than force control so they are different from the previously discussed "snap-through" in Fig. 6(d). As the equivalent constraint stiffness k^* increases, the energy barrier of deforming from '2-1' stable state to 'p' configuration increases significantly (ΔE_e in Fig. 7(b) and (c), second row); however, the energy barrier of the opposite switch from '2-2' to 'r' does not change as much (ΔE_c in Fig. 7(b) and (c)). Hence, when with a relatively large value of k^*, the energy barrier of extension from states '2-1' to '2-2' significantly outstrips that of the opposite switch (i.e. $\Delta E_e \gg \Delta E_c$), generating the strong asymmetry. Moreover, the energy barrier of the switch between the '1-1' and '2-1' states does not change significantly since the potential energy path between these two states

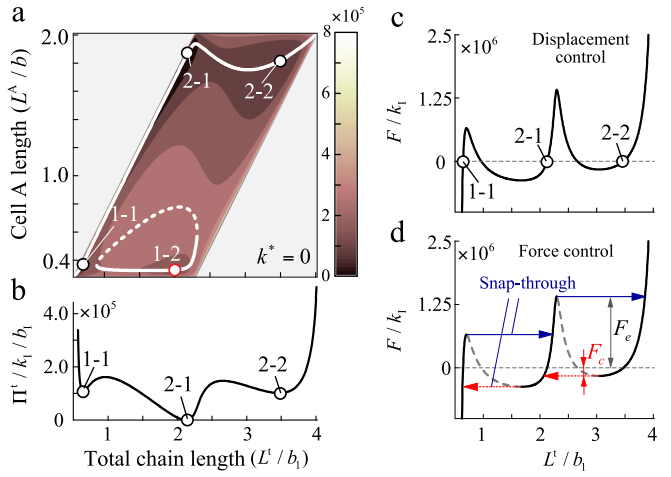

Fig. 6. The energy landscape and corresponding reaction force of a sample dual-cell chain assuming k^* is zero. (a) Total energy contour, the darker the color the lower the energy. Solid curves denote the potential energy paths, which are the energy minima at a given total chain length; and the dashed line correspond to energy maxima. The gray shaded regions are physically unachievable. (b) The total energy landscape along the energy path that connects the three stable states. (c) Reaction force–displacement relationship based on the displacement control method. (d) Force–displacement relationship based on the force control method. Note the contour legend of (a) also applies to Figs. 7 and 9.

remain continuous, and it remains significantly smaller than ΔE_e. As a result of the aforementioned asymmetrical energy barriers, the external force required to switch the dual cell chain from the stable '2-1' state toward '2-2' state also increases significantly as k^* increases (F_e in the third row of Fig. 7). However, the required compression force to switch the dual-cell chain from '2-2' back toward '2-1' state does not increase as much and is much lower than F_e (F_c in the third row of Fig. 7, $F_e \gg F_c$).

In our experiment, the film-connection apply a stronger constraint on the relative folding between the two unit cells than the rod-connection, which can be characterized as an increase of the effective stiffness k^*. Therefore, the theoretical analyses above can qualitatively explain the asymmetric behaviors observed in the experiments, especially regarding the critical forces for compression and extension switch. The consistency between experiment and analysis also validates that the spine angles and the equivalent constraint energy can effectively reveal the underlying physical principles.

Our analytical investigation elucidates the importance of the three-dimensional nature of origami folding. The kinematic constraint discussed in (Eqs. (5)–(7)) is a result of the coupling between unit cell length change in z-axis and the connecting creases displacement along x and y-axes at the boundary between two cells. Thus, the 3D deformation of the unit cells plays the key role in achieving asymmetric energy barrier.

Another important observation from our analytical examination is the correlation between the asymmetric energy barriers and the strength of the kinematic constraint from the connecting zig-zag creases. As k^*increases, the ratio of both $\Delta E_e/\Delta E_c$ and F_e/F_c increases (Fig. 8(a, b)). Note that if k^* is sufficiently large, the potential energy paths calculated by the equivalent energy model (Eq. (8)) will converge to the deformation paths based on the ideal rigid-folding assumption (i.e. $\psi^A = \psi^B$). One can thus deduce that a sufficiently strong kinematic constraint between the two adjacent unit cells can effectively create a *diode effect*, so that the dual cell chain can be easily compressed via switching from '2-2' to '2-1' stable states, but demand a large force to be extended by the opposite switch (Fig. 8(b)).

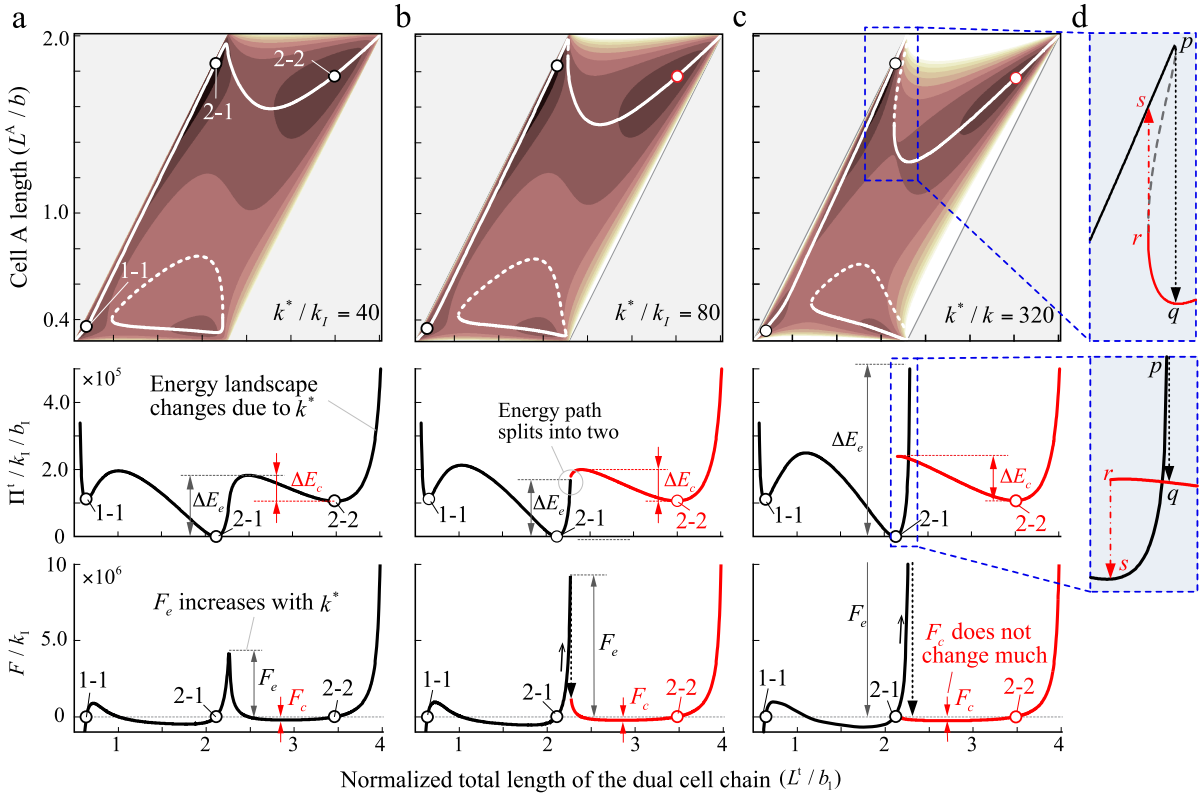

Fig. 7. The energy contours (first row), energy landscapes (second row), and the corresponding reaction forces (third row) change fundamentally with the increase of effective constraint stiffness k^*: (a) $k^*/k_1 = 40$, (b) $k^*/k_1 = 80$, and (c) $k^*/k_1 = 320$. (d) Blow-up view of the energy landscapes in (c) that the potential energy path between '2-1' and '2-2' splits and overlaps.

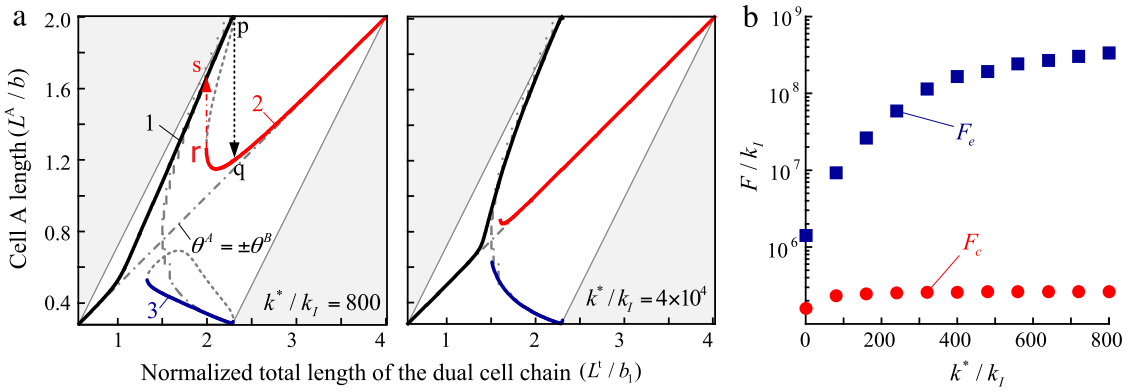

Fig. 8. Potentials to achieve a static mechanical diode effect. (a) The energy paths corresponding to increasingly large k^* values: $k^*/k_1 = 800$ and $k^*/k_1 = 4 \times 10^4$. Solid lines are potential energy paths corresponding to the energy minima. The dash-dotted lines are the deformation path based on ideal-fold folding assumption ($\psi^A = \psi^B$, Fig. 4(b)). (b): Relationships between the critical forces (F_e, F_c) and strength of the folding induced kinematic constraints (k^*). Results are from the equivalent model defined by Eq. (8). F_e increases monotonically with k^* while F_c remains almost unchanged.

Harnessing nonlinear elastic properties to achieve diode-like mechanical behaviors is an increasingly important subject of research [58–61]. In particular, it has been shown that multi-stable structures and materials with carefully designed micro-architectures can achieve unidirectional acoustic [62] and elastic [27,28] wave propagation. However, previous studies have been focusing on dynamic responses involving wave propagation, while static diode effect is still a nascent topic [63]. The reported asymmetric energy barriers from the multi-stable origami provides a pathway to achieve strong and static diode effect. This effect can rectify reciprocal external forces into unidirectional deformations, which can open new possibilities for developing multi-functional metamaterials and structures.

5. Further case studies

Results from the previous sections are based on one particular example of dual-cell chain design where $\theta_o^A = 60°$ and $\theta_o^B = -60°$ so that $F_e^A < F_e^B$ and $F_c^A > F_c^B$. Choosing different origami designs in terms of the stress-free folding angles, crease stiffness, and Miura-ori geometry can generate fundamentally different energy contours and force–displacement relationships, yet the asymmetric energy barriers and static mechanical diode effect can still be evident. For example, one can choose the stress free folding angles of the two cells to be $\theta_o^A = -60°$ and $\theta_o^B = -70°$ so that there are still four stable states but $F_c^A < F_c^B$. Such a difference in the critical force relationships can lead to a different switching sequence. The energy contours, energy landscapes, and force–displacement relationship of this dual cell chain based on different k^* values are shown in Fig. 9. When $k^* = 0$, there exist two potential energy paths, each connecting two stable states (Fig. 9(a)). Therefore, as the dual-cell chain is monotonically extended or compressed based on displacement control, it will jump between the two energy paths. For example, starting from the '1-1' state, monotonically extending the dual-cell chain will make it follow the path of '1-1'→ '2-1'→p →q →'2-2'. On the other hand, monotonically compressing the dual-cell chain from the '2-2' state will make it follow the path of '2-2'→ '1-2'→r →s →'1-1' (first two rows of Fig. 9(a)). As k^* increases to a critical value, the energy path connecting the '1-2' and '2-2' states splits into two separate ones, and the jump between different potential energy paths become quite complex. For example, when $k^*/k_1 = 320$ as in Fig. 9(d), monotonic extension from the '1-1' state will follow the path of '1-1'→ '2-1'→p →q →'2-2'; monotonic extension from the '1-2' state will follow the path of '1-2'→p^*→q →'2-2'; and monotonic compression from the '2-2' state will follow the path of '2-2'→u →v →r →s →'1-1', where the '1-2' state will be skipped.

Nonetheless, as k^*increases, the required extension force to switch the dual-cell chain from either '1-2' or '2-1' state to the '2-2' state increases significantly, while the compression force required for the opposite switches does not increase much so that $F_{e1} \gg F_c$, $F_{e2} \gg F_c$ (third row of Fig. 9). Here F_{e1} corresponds to the required extension force for extensional '2-1' → '2-2' switch, and F_{e2} corresponds to the required extension force for extensional '1-2'→ '2-2' switch. Thus the newly uncovered asymmetric energy barrier and the static diode effects at these two stable states are still evident even with the different dual-cell chain design.

6. Summary and discussion

This study reports and examines a folding-induced, asymmetric energy barrier in a multi-stable stacked origami cellular solid. The origami unit cell – consisting of two Miura-ori sheets with different geometric designs and crease stiffness – can be bistable due to the nonlinear relationships between the crease rotation and the overall folding. These bistable cells can be assembled into a cellular solid that possesses multiple stable states with different internal folding configurations. The zig-zag shaped connecting creases between adjacent unit cells can couple their three-dimensional folding deformations, imparting a unique kinematic constraint that does not exist in the lower dimensional bistable mechanisms. Experiment observation on dual-cell chains reveal that this kinematic constraint can increase the energy barrier of the extension switch between certain stable states without significantly changing the barrier of the opposite compression switch, incurring a unique asymmetry. We formulate an analytical model to examine the underlying principles by introducing equivalent constraint stiffness, which is associated with the spine angle mismatch at the connecting creases between two adjacent cells. Our analyses revealed that a sufficiently large constraint stiffness can fundamentally alter the energy landscape of the dual cell chain and introduce the asymmetric energy barrier. Analytical results also imply that, via strengthening the kinematic constraint, we can achieve a static mechanical diode effect. Therefore, if many origami cells are assembled into a cellular solid, it could be easily compressed via switching between certain stable states, but demand a large external force to be extended. This kind of static diode effect can be harnessed for many novel applications such as motion rectifying and wave propagation control.

Acknowledgments

S. Li acknowledges the support by the National Science Foundation (award # CMMI-1633952) and the startup funding from

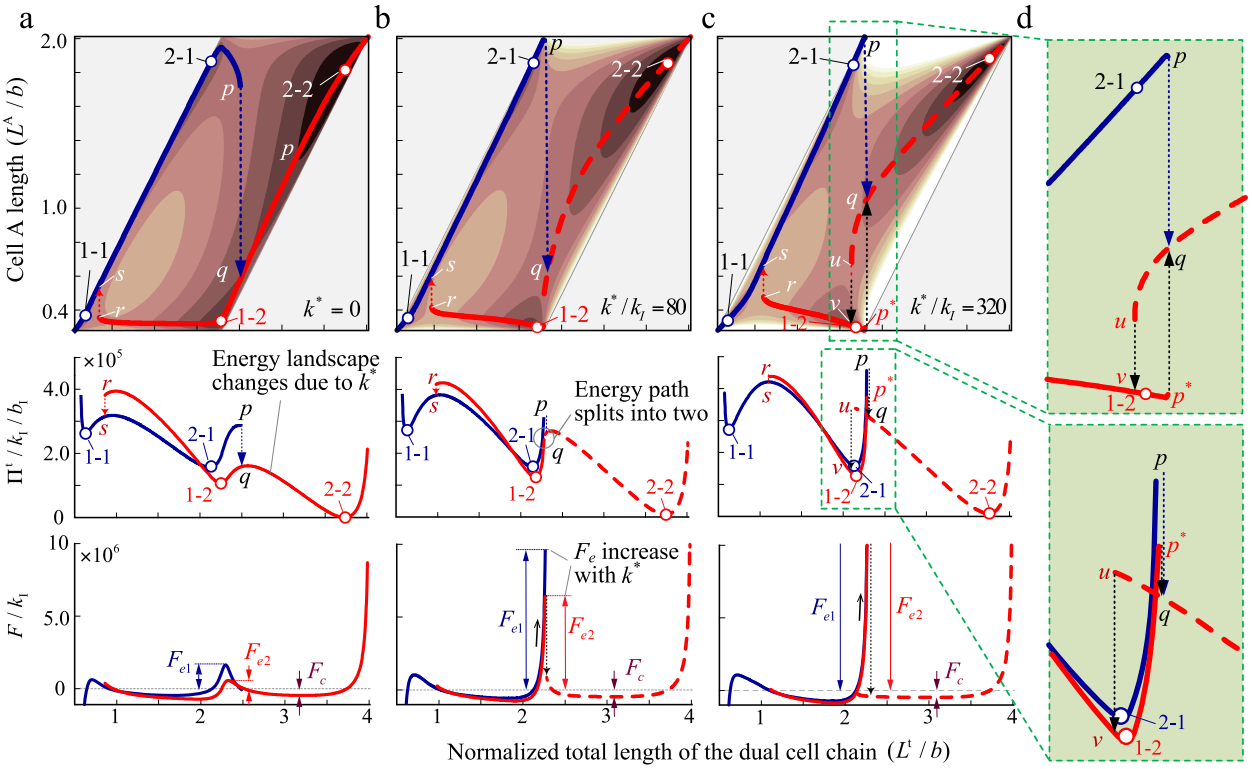

Fig. 9. The energy contour, landscape and corresponding reaction force with increasing equivalent constraint stiffness k^*, (a) $k^* = 0$;(b) $k^*/k_l = 80$; (c) $k^*/k_l = 320$. In these cases $\theta_o^A = -60°$, $\theta_o^B = -70°$. For clarity, only the energy minimum is plotted in the contour map. As the equivalent constraint stiffness k^* increases, both F_{e1} and F_{e2} increase significantly, indicating the existence of the asymmetric multistability and the mechanical diode effect. The contour legend in the first row is the same as that in Fig. 6(a). For clarity, (d) shows the blow-up view of the energy landscapes at the complex transitions.

the Clemson University. H. Fang and K.W. Wang acknowledge the support by the National Science Foundation (award # CMMI-1634545) and the University of Michigan Collegiate Professorship.

References

[1] S.W. Kim, J.S. Koh, J.G. Lee, J. Ryu, M. Cho, K.J. Cho, Flytrap-inspired robot using structurally integrated actuation based on bistability and a developable surface, Bioinspir. Biomim. 9 (2014) 36004. http://dx.doi.org/10.1088/1748-3182/9/3/036004.

[2] J. Sun, Q. Guan, Y. Liu, J. Leng, Morphing aircraft based on smart materials and structures: A state-of-the-art review, J. Intell. Mater. Syst. Struct. 27 (2016) 2289–2312. http://dx.doi.org/10.1177/1045389X16629569.

[3] X. Lachenal, S. Daynes, P.M. Weaver, Review of morphing concepts and materials for wind turbine blade applications, Wind Energy 16 (2013) 283–307. http://dx.doi.org/10.1002/we.531.

[4] S. Daynes, P.M. Weaver, Review of shape-morphing automobile structures: concepts and outlook, Proc. Inst. Mech. Eng. D 227 (2013) 1603–1622. http://dx.doi.org/10.1177/0954407013496557.

[5] N. Kidambi, R.L. Harne, K.W. Wang, Adaptation of energy dissipation in a mechanical metastable module excited near resonance, J. Vib. Acoust. 138 (2015) 11001. http://dx.doi.org/10.1115/1.4031411.

[6] R.L. Harne, Z. Wu, K.W. Wang, Designing and harnessing the metastable states of a modular metastructure for programmable mechanical properties adaptation, J. Mech. Des. 138 (2015) 21402. http://dx.doi.org/10.1115/1.4032093.

[7] Z. Wu, R.L. Harne, K.W. Wang, Exploring a modular adaptive metastructure concept inspired by muscles cross-bridge, J. Intell. Mater. Syst. Struct. 27 (2016) 1189–1202. http://dx.doi.org/10.1177/1045389X15586451.

[8] B. Florijn, C. Coulais, M. van Hecke, Programmable mechanical metamaterials, Phys. Rev. Lett. 113 (2014) 175503. http://dx.doi.org/10.1103/PhysRevLett.113.175503.

[9] J.N. Grima, R. Caruana-Gauci, M.R. Dudek, K.W. Wojciechowski, R. Gatt, Smart metamaterials with tunable auxetic and other properties, Smart Mater. Struct. 22 (2013) 84016. http://dx.doi.org/10.1088/0964-1726/22/8/084016.

[10] R.L. Harne, K.W. Wang, Harnessing Bistable Structural Dynamics: for Vibration Control, Energy Harvesting and Sensing, first ed., John Wiley and Sons, 2017. https://goo.gl/GFTEUA. (Accessed 15 January 2017).

[11] D.R. Johnson, M. Thota, F. Semperlotti, K.W. Wang, On achieving high and adaptable damping via a bistable oscillator, Smart Mater. Struct. 22 (2013) 115027. http://dx.doi.org/10.1088/0964-1726/22/11/115027.

[12] H. Fang, K.W. Wang, Piezoelectric vibration-driven locomotion systems—exploiting resonance and bistable dynamics, J. Sound Vib. 391 (2017) 153–169. http://dx.doi.org/10.1016/j.jsv.2016.12.009.

[13] D.R. Johnson, R.L. Harne, K.W. Wang, A disturbance cancellation perspective on vibration control using a bistable snap-through attachment, J. Vib. Acoust. 136 (2014) 31006. http://dx.doi.org/10.1115/1.4026673.

[14] K. Yang, R.L. Harne, K.W. Wang, H. Huang, Dynamic stabilization of a bistable suspension system attached to a flexible host structure for operational safety enhancement, J. Sound Vib. 333 (2014) 6651–6661. http://dx.doi.org/10.1016/j.jsv.2014.07.033.

[15] R.L. Harne, K.W. Wang, A review of the recent research on vibration energy harvesting via bistable systems, Smart Mater. Struct. 22 (2013) 23001. http://dx.doi.org/10.1088/0964-1726/22/2/023001.

[16] S.P. Pellegrini, N. Tolou, M. Schenk, J.L. Herder, Bistable vibration energy harvesters: A review, J. Intell. Mater. Syst. Struct. 24 (2013) 1303–1312. http://dx.doi.org/10.1177/1045389X12444940.

[17] M.F. Daqaq, R. Masana, A. Erturk, D. Dane Quinn, On the role of nonlinearities in vibratory energy harvesting: A critical review and discussion, Appl. Mech. Rev. 66 (2014) 40801. http://dx.doi.org/10.1115/1.4026278.

[18] R.L. Harne, K.W. Wang, A bifurcation-based coupled linear-bistable system for microscale mass sensing, J. Sound Vib. 333 (2014) 2241–2252. http://dx.doi.org/10.1016/j.jsv.2013.12.017.

[19] R.L. Harne, K.W. Wang, Passive measurement of progressive mass change via bifurcation sensing with a multistable micromechanical system, J. Intell. Mater. Syst. Struct. 26 (2015) 1622–1632. http://dx.doi.org/10.1177/1045389X14546781.

[20] G. Puglisi, L. Truskinovsky, Mechanics of a discrete chain with bi-stable elements, J. Mech. Phys. Solids 48 (2000) 1–27. http://dx.doi.org/10.1016/S0022-5096(99)00006-X.

[21] G. Puglisi, L. Truskinovsky, Rate independent hysteresis in a bi-stable chain, J. Mech. Phys. Solids 50 (2002) 165–187. http://dx.doi.org/10.1016/S0022-5096(01)00055-2.

[22] I. Benichou, S. Givli, Structures undergoing discrete phase transformation, J. Mech. Phys. Solids 61 (2013) 94–113. http://dx.doi.org/10.1016/j.jmps.2012.08.009.

[23] S. Shan, S.H. Kang, J.R. Raney, P. Wang, L. Fang, F. Candido, J.A. Lewis, K. Bertoldi, Multistable architected materials for trapping elastic strain energy, Adv. Mater. 27 (2015) 4296–4301. http://dx.doi.org/10.1002/adma.201501708.
[24] T. Frenzel, C. Findeisen, M. Kadic, P. Gumbsch, M. Wegener, Tailored buckling microlattices as reusable light-weight shock absorbers, Adv. Mater. 28 (2016) 5865–5870. http://dx.doi.org/10.1002/adma.201600610.
[25] D. Restrepo, N.D. Mankame, P.D. Zavattieri, Phase transforming cellular materials, Extrem. Mech. Lett. 4 (2015) 52–60. http://dx.doi.org/10.1016/j.eml.2015.08.001.
[26] K. Che, C. Yuan, J. Wu, H.J. Qi, J. Meaud, Three-dimensional-printed multistable mechanical metamaterials with a deterministic deformation sequence, J. Appl. Mech. 84 (2016) 11004. http://dx.doi.org/10.1115/1.4034706.
[27] J.R. Raney, N. Nadkarni, C. Daraio, D.M. Kochmann, J.A. Lewis, K. Bertoldi, Stable propagation of mechanical signals in soft media using stored elastic energy, Proc. Natl. Acad. Sci. (2016) 201604838. http://dx.doi.org/10.1073/pnas.1604838113.
[28] N. Nadkarni, A.F. Arrieta, C. Chong, D.M. Kochmann, C. Daraio, Unidirectional transition waves in bistable lattices, Phys. Rev. Lett. 116 (2016) 244501. http://dx.doi.org/10.1103/PhysRevLett.116.244501.
[29] B. Haghpanah, L. Salari-Sharif, P. Pourrajab, J. Hopkins, L. Valdevit, Multistable shape-reconfigurable architected materials, Adv. Mater. 28 (2016) 7915–7920. http://dx.doi.org/10.1002/adma.201601650.
[30] M. McArthur, R.J. Lang, Folding Paper: The Infinite Possibilities of Origami, first ed., Tuttle Publishing, Rutland VT, USA, 2013. https://goo.gl/RZE1xH.
[31] M. Schenk, A.D. Viquerat, K.A. Seffen, S.D. Guest, Review of inflatable booms for deployable space structures: packing and rigidization, J. Spacecr. Rockets 51 (2014) 762–778. http://dx.doi.org/10.2514/1.A32598.
[32] T. Tachi, Rigid foldable thick origami, in: P. Wang-Iverson, R.J. Lang, M. Yim (Eds.), Origami 5, first ed., A K Peters/CRC Press, Boca Raton, FL, USA, 2011, pp. 253–264. https://goo.gl/Wszi9K.
[33] Y. Chen, R. Peng, Z. You, Origami of thick panels, Science 349 (2015) 396–400. http://dx.doi.org/10.1126/science.aab2870.
[34] E.T. Filipov, T. Tachi, G.H. Paulino, Origami tubes assembled into stiff, yet reconfigurable structures and metamaterials, Proc. Natl. Acad. Sci. 112 (2015) 12321–12326. http://dx.doi.org/10.1073/pnas.1509465112.
[35] S. Felton, M. Tolley, E.D. Demaine, D. Rus, R. Wood, A method for building self-folding machines, Science 345 (2014) 644–646. http://dx.doi.org/10.1126/science.1252610.
[36] S. Miyashita, S. Guitron, M. Ludersdorfer, C.R. Sung, D. Rus, An untethered miniature origami robot that self-folds, walks, swims, and degrades, in: 2015 IEEE Int. Conf. Robot. Autom. IEEE, 2015, pp. 1490–1496. http://dx.doi.org/10.1109/ICRA.2015.7139386.
[37] A. Firouzeh, J. Paik, Robogami: A fully integrated low-profile robotic origami, J. Mech. Robot. 7 (2015) 21009. http://dx.doi.org/10.1115/1.4029491.
[38] C.L. Randall, E. Gultepe, D.H. Gracias, Self-folding devices and materials for biomedical applications, Trends Biotechnol. 30 (2012) 138–146. http://dx.doi.org/10.1016/j.tibtech.2011.06.013.
[39] M. Johnson, Y. Chen, S. Hovet, S. Xu, B. Wood, H. Ren, J. Tokuda, Z.T.H. Tse, Fabricating biomedical origami: a state-of-the-art review, Int. J. Comput. Assist. Radiol. Surg. (2017). http://dx.doi.org/10.1007/s11548-017-1545-1.
[40] K.C. Cheung, T. Tachi, S. Calisch, K. Miura, Origami interleaved tube cellular materials, Smart Mater. Struct. 23 (2014) 94012. http://dx.doi.org/10.1088/0964-1726/23/9/094012.
[41] H. Yasuda, J. Yang, Reentrant origami-based metamaterials with negative Poisson's ratio and bistability, Phys. Rev. Lett. 114 (2015) 185502. http://dx.doi.org/10.1103/PhysRevLett.114.185502.
[42] M. Schenk, S.D. Guest, Geometry of Miura-folded metamaterials, Proc. Natl. Acad. Sci. 110 (2013) 3276–3281. http://dx.doi.org/10.1073/pnas.1217998110.
[43] C. Lv, D. Krishnaraju, G. Konjevod, H. Yu, H. Jiang, Origami based mechanical metamaterials, Sci. Rep. 4 (2014) 5979. http://dx.doi.org/10.1038/srep05979.
[44] J.T.B. Overvelde, T.A. de Jong, Y. Shevchenko, S.A. Becerra, G.M. Whitesides, J.C. Weaver, C. Hoberman, K. Bertoldi, A three-dimensional actuated origami-inspired transformable metamaterial with multiple degrees of freedom, Nature Commun. 7 (2016) 10929. http://dx.doi.org/10.1038/ncomms10929.
[45] M. Eidini, G.H. Paulino, Unraveling metamaterial properties in zigzag-base folded sheets, Sci. Adv. 1 (2015) e1500224–e1500224. http://dx.doi.org/10.1126/sciadv.1500224.
[46] H. Fang, S. Li, K.W. Wang, vertex origami structures, Proc. R. Soc. Lond. Ser. A Math. Phys. Eng. Sci. 472 (2016) 20160682. http://dx.doi.org/10.1098/rspa.2016.0682.
[47] H. Fang, S. Li, H. Ji, K.W. Wang, Uncovering the deformation mechanisms of origami metamaterials by introducing generic degree-four vertices, Phys. Rev. E 94 (2016) 43002. http://dx.doi.org/10.1103/PhysRevE.94.043002.
[48] S. Li, K.W. Wang, Fluidic origami: a plant-inspired adaptive structure with shape morphing and stiffness tuning, Smart Mater. Struct. 24 (2015) 105031. http://dx.doi.org/10.1088/0964-1726/24/10/105031.
[49] S. Li, K.W. Wang, Fluidic origami with embedded pressure dependent multistability: a plant inspired innovation, J. R. Soc. Interface. 12 (2015) 20150639. http://dx.doi.org/10.1098/rsif.2015.0639.
[50] S. Waitukaitis, R. Menaut, B.G. Chen, M. van Hecke, Origami multistability: from single vertices to metasheets, Phys. Rev. Lett. 114 (2015) 55503. http://dx.doi.org/10.1103/PhysRevLett.114.055503.
[51] J.L. Silverberg, A.A. Evans, L. McLeod, R.C. Hayward, T.C. Hull, C.D. Santangelo, I. Cohen, Using origami design principles to fold reprogrammable mechanical metamaterials, Science 345 (2014) 647–650. http://dx.doi.org/10.1126/science.1252876.
[52] J.L. Silverberg, J.H. Na, A.A. Evans, B. Liu, T.C. Hull, C.D. Santangelo, R.J. Lang, R.C. Hayward, I. Cohen, Origami structures with a critical transition to bistability arising from hidden degrees of freedom, Nature Mater. 14 (2015) 389–393. http://dx.doi.org/10.1038/nmat4232.
[53] B.H. Hanna, J.M. Lund, R.J. Lang, S.P. Magleby, L.L. Howell, Waterbomb base: a symmetric single-vertex bistable origami mechanism, Smart Mater. Struct. 23 (2014) 94009. http://dx.doi.org/10.1088/0964-1726/23/9/094009.
[54] S. Li, Anisotroipic, adaptive, and asymmetric nulti-stability from origami folding, in: Proc. ASME IDETC/CIE, Clevaland, OH, 2017, p. IDETC-67285.
[55] H. Fang, S. Li, H. Ji, K.W. Wang, Dynamics of a bistable miura-origami structure, Phys. Rev. E 95 (2017) 52211. http://dx.doi.org/10.1103/PhysRevE.95.052211.
[56] N. Yang, J.L. Silverberg, Decoupling local mechanics from large-scale structure in modular metamaterials, Proc. Natl. Acad. Sci. (2017) 201620714. http://dx.doi.org/10.1073/pnas.1620714114.
[57] S. Li, H. Fang, K.W. Wang, Recoverable and programmable collapse from folding pressurized origami cellular solids, Phys. Rev. Lett. 117 (2016) 114301. http://dx.doi.org/10.1103/PhysRevLett.117.114301.
[58] B. Liang, X.S. Guo, J. Tu, D. Zhang, J.C. Cheng, An acoustic rectifier, Nature Mater. 9 (2010) 989–992. http://dx.doi.org/10.1038/nmat2881.
[59] B.I. Popa, S.A. Cummer, Non-reciprocal and highly nonlinear active acoustic metamaterials, Nature Commun. 5 (2014) 1–5. http://dx.doi.org/10.1038/ncomms4398.
[60] X. Zhu, X. Zou, B. Liang, J. Cheng, One-way mode transmission in one-dimensional phononic crystal plates, J. Appl. Phys. 108 (2010) 124909. http://dx.doi.org/10.1063/1.3520491.
[61] N. Boechler, G. Theocharis, C. Daraio, Bifurcation-based acoustic switching and rectification, Nature Mater. 10 (2011) 665–668. http://dx.doi.org/10.1038/nmat3072.
[62] O.R. Bilal, A. Foehr, C. Daraio, Bistable metamaterial for switching and cascading elastic vibrations, Proc. Natl. Acad. Sci. (2017) 201618314. http://dx.doi.org/10.1073/pnas.1618314114.
[63] C. Coulais, D. Sounas, A. Alù, Static non-reciprocity in mechanical metamaterials, Nature 542 (2017) 461–464. http://dx.doi.org/10.1038/nature21044.